Accuracy of the Cell-Centered Grid Metric in the DLR TAU-Code

Axel Schwöppe and Boris Diskin

Abstract. The drag prediction accuracy of the current version of the cell-centered grid metric discretization in the edge-based flow solver TAU lags behind the accuracy of the cell-vertex grid metric on highly-skewed unstructured meshes. Inaccurate convective fluxes and gradients contributing to the turbulence sources are identified as the reasons for this accuracy degradation. Alternative approaches for cell-centered discretizations are presented and shown to lead to significant accuracy and robustness improvements. Recommendations are given to improve spatial discretization schemes for the cell-centered grid metric in an edge-based finite volume code.

1 Introduction

Both cell-centered and cell-vertex discretizations are widely used for turbulent flow-simulations in aerospace applications. The relative advantages of the two approaches have been studied concerning accuracy, efficiency and robustness, but a consensus has not emerged [3, 4, 7].

The DLR RANS-Solver TAU [10] is an unstructured CFD solver based on a finite-volume discretization scheme. The geometry of a configuration is mapped by a cell-vertex grid metric and stored via an edge-based data structure. Since Release 2008.1.0 of the TAU-code, a cell-centered grid metric based on the same data structure is available as well. The drag prediction accuracy of the current cell-centered version of the TAU-Code lags behind the accuracy of the cell-vertex version for

Axel Schwöppe
Deutsches Zentrum für Luft und Raumfahrt e.V., Lilienthalplatz 7,
38108 Braunschweig, Germany
e-mail: axel.schwoeppe@dlr.de

Boris Diskin
National Institute of Aerospace (NIA), 100 Exploration Way, Hampton, VA 23681, USA
e-mail: bdiskin@nianet.org

A. Dillmann et al. (Eds.): *New Results in Numer. & Exp. Fluid Mech.*, NNFM 121, pp. 429–437.
DOI: 10.1007/978-3-642-35680-3_51

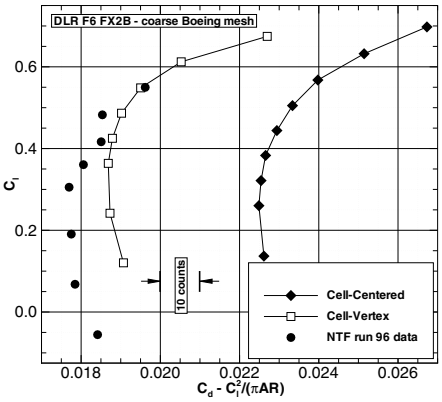

Fig. 1 Idealized drag polar of DLR F6 configuration at Mach 0.75 and Re = 5.000.000 [12] on a coarse mesh (provided by Boeing) for cell-vertex (upwind scheme, least-squares gradients) and cell-centered (upwind scheme, Green-Gauss gradients) grid metric. The original Spalart-Allmaras turbulence model is used. Circles represent wind-tunnel measurements conducted at the National Transonic Facility.

complex industrial three-dimensional (3-D) configurations. On the other side, test cases (e.g. NACA0012, flat plate) using high quality meshes, which are nearly orthogonal in relevant mesh regions, show no significant differences between grid metrics.

A test case from the Third AIAA Drag Prediction Workshop (DPW-III) is chosen to illustrate and explain the reasons for this accuracy degradation. The case is the DLR F6 wing-body configuration [12]. A comparison of the idealized drag polar computed on an unstructured, highly-skewed mesh is shown in Fig. 1. The mesh is the coarse mesh of the family used in the DPW-III computations for a mesh convergence study. Differences of more than 30 drag counts have been observed between the cell-vertex and the cell-centered solutions; the cell-vertex solution is in much better agreement with the wind-tunnel measurements.

This paper presents explanations for the insufficient accuracy of the cell-centered solution and offers approaches to improve this accuracy. Section 2 considers details of the spatial grid-metric discretizations relying on the edge-based data structure of the TAU-code. The gradient calculation methods used in the current TAU-code and improved approaches for the cell-centered grid metric are described in Section 3. Conclusions and recommendations for cell-centered finite volume flow solvers based on an edge-based date structure are offered in Section 4.

2 Spatial Discretization

The accuracy difference is observed in a steady case solution and, thus, has its roots in the spatial discretization. The spatial discretization used in the TAU-code is derived from the integral form of the 3-D RANS equations

$$\frac{\partial}{\partial t}\int_{\Omega}\mathbf{W}d\Omega+\oint_{\partial\Omega}(\mathbf{F}_c-\mathbf{F}_v)\,dS=\int_{\Omega}\mathbf{Q}d\Omega. \tag{1}$$

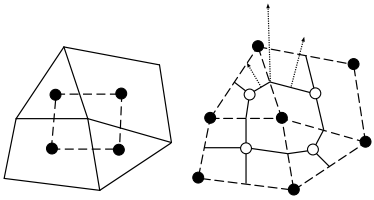

(a) Cell-Centered (b) Cell-Vertex

Fig. 2 Computational mesh for cell-vertex and cell-centered grid metric. Black circles represent locations of degrees of freedom, white circles represent vertices of the control volumes, solid lines denote faces of the control volumes, dashed lines denote edges, and arrows denote area-normal vectors.

Here, t is the time, Ω is the spatial domain, $\mathbf{W}$ is the vector of the conservative Reynolds-averaged variables including main and turbulence variables, $\mathbf{F}_c$ and $\mathbf{F}_v$ are the respective vectors of convective and viscous fluxes, and $\mathbf{Q}$ is the source term. The discretization of the governing equations follows the method of lines, which decouples the spatial and the temporal discretization [2]. The spatial domain is divided into a set of non-overlapping polyhedral control volumes, and Eq. 1 is discretized for each control volume. The finite-volume discretization of Eq.1 at a representative control volume i can be written as

$$\frac{d\mathbf{W}_i}{dt} = -\frac{1}{\Omega_i}\left[\sum_{j=1}^{N}(\mathbf{F}_c - \mathbf{F}_v)_{ij}\,\mathbf{n}_{ij} - \mathbf{Q}_i\Omega_i\right], \tag{2}$$

where $\mathbf{n}_{ij}$ is the area-normal vector of the control volume face separating points i and j, and N is the number of face-neighbors of control volume i. The area-normal vector is the outward vector perpendicular to the face with the magnitude equal to the face area. The connection between point i and j is denoted as edge ij.

The set of non-overlapping polyhedral control volumes is called the computational or dual mesh. The computational mesh is dependent on the used grid metric and is based on the primary mesh, containing tetrahedrons, hexahedrons, prisms and pyramids in the context of the TAU-code. For the cell-centered grid metric, degrees of freedom are located at the centers of the primal cells. The cell center coordinates are typically defined as the averages of the cell vertex coordinates. The control volumes are the primal cells (Fig. 2(a)). For the cell-vertex grid metric, degrees of freedom are located at the vertices of the primal cells. The control volumes are constructed around the vertices by the median-dual partition: the centers of primal cells are connected with the midpoints of the surrounding faces, the area-normals can be computed as the vector sum of the area-normals of the faces adjacent to the edge (Fig. 2(b)).

There are at least two reasons for the difference between the cell-vertex and the cell-centered solutions: (1) accuracy of the surface flux integration and (2) accuracy of the gradients contributing to the source of the turbulence equation. In this section,

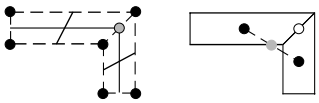

(a) Cell-Vertex (b) Cell-Centered

Fig. 3 Possible locations of edge-midpoints (gray circles) and face-integration points (white circles) in a typical unstructured discretization, e.g. of a blunt trailing edge. Black lines represent control volume faces, dashed lines edges, black circles locations of degrees of freedom.

accuracy of the surface flux integration is considered; the effect of gradient approximation on the turbulent sources and solution accuracy is discussed in Section 3.

The surface integral of Eq. 1 is approximated via the sum of fluxes over control volume faces in Eq. 2. At each control volume face, the flux is reconstructed at the face-integration point and multiplied by the area-normal vector. For second-order accuracy, the reconstruction at the face-integration points should be second order accurate. In an edge-based code, the values are typically reconstructed at an edge-midpoint and used to approximate values at a face-integrations point. In a cell-vertex code, the edge-midpoints coincide with the face-integration points (Fig. 3(a)). In a cell-centered code, on highly-stretched curved grids, the locations of the corresponding edge-midpoint and face-integration point may differ significantly (Fig. 3(b)). This difference has been identified as the leading reason for inaccuracy of the order discussed in this paper.

In the TAU-code, there are two second-order schemes for the convective fluxes: a central scheme with artificial dissipation and an upwind scheme [2]. The central scheme averages flow variables and adds an artificial dissipation term to avoid odd-even decoupling.

$$\mathbf{F}_{ij} = \frac{1}{2}\left(\mathbf{W}_i + \mathbf{W}_j\right) + \mathbf{D}_{ij}. \tag{3}$$

Details concerning the dissipation term D_{ij} can be found e.g. in [2]. The average of the control volume values W_i and W_j is intended to provide a solution approximation at the face-integration point. In the case of the cell-centered grid metric, this average introduces an error caused by the difference between the locations of the face-integration point and edge-midpoint (Fig. 3(b)) and thus reduces the order of the scheme. This error can only be avoided if additional neighboring points are involved to get a more accurate interpolation at the face-integration point. Due to the current edge-based data structure of the TAU-code, no information about other neighboring points is available for the cell-centered metric. Thus, the central scheme is not recommended for edge-based cell-centered grid metric without altering the edge-based data structure significantly.

The upwind scheme reconstructs the fluxes at the face-integration point at the left and the right side of the face.

$$\mathbf{F}_{ij} = \frac{1}{2}\left(\mathbf{F}_L + \mathbf{F}_R - \left|\mathbf{A}_{ij}\right|\left(\mathbf{W}_R - \mathbf{W}_L\right)\right). \tag{4}$$

$\mathbf{F}_L$ and $\mathbf{F}_R$ are the left and right fluxes respectively, computed from the state solutions reconstructed at the corresponding side of the face, $\mathbf{A}_{ij}$ denotes the convective flux Jacobian. The state solutions are reconstructed at the face-integration point with second order using the solutions and solution gradients defined at the control-volume centers. The gradient accuracy has to be at least first order [2]. The upwind scheme, Eq. 4, is usable for the edge-based cell-centered grid metric.

3 Gradient Computation

Two types of gradients are used in the finite-volume discretization schemes: cell gradients are used in second-order upwind schemes and in source terms for turbulence models, face gradients are used to compute viscous fluxes.

Face-gradients are used to evaluate the viscous fluxes $\mathbf{F}_v$ in Eq. 2. The derivatives of the velocity components and the temperature have to be known at the faces of the control volumes. The schemes for computing the face gradients strongly affect robustness of the solution process on highly-skewed meshes.

With an edge-based data structure, an average of the corresponding cell-gradients ∇W_i is typically calculated to compute the face gradients

$$\overline{\nabla W}_{ij} = \frac{1}{2}\left(\nabla W_i + \nabla W_j\right). \tag{5}$$

Hasselbacher [6] observed that such averaging leads to odd-even decoupling and introduced edge-derivative augmentation to improve robustness. It was suggested that the edge derivative can be introduced in two ways: as either edge-normal or face-tangent augmentation. The more widely used edge-normal augmentation is implemented in the TAU-code. The effects of both augmentations have been studied in [9, 11]. Face-tangent augmentation has been recommended as more robust.

The edge-normal augmentation is defined as

$$\nabla W|_{ij} = \overline{\nabla W}_{ij} - [\overline{\nabla W}_{ij} \cdot \hat{\mathbf{e}}_{ij} - \frac{W_j - W_i}{|\mathbf{e}_{ij}|}]\hat{\mathbf{e}}_{ij}, \tag{6}$$

where $\mathbf{e}_{ij}$ is the edge vector and $\hat{\mathbf{e}}_{ij}$ is the normalized edge vector. The face-tangent augmentation is defined as

$$\nabla W|_{ij} = \overline{\nabla W}_{ij} - [\overline{\nabla W}_{ij} \cdot \hat{\mathbf{e}}_{ij} - \frac{W_j - W_i}{|\mathbf{e}_{ij}|}]\frac{\hat{\mathbf{n}}_{ij}}{\hat{\mathbf{n}}_{ij} \cdot \hat{\mathbf{e}}_{ij}}, \tag{7}$$

where $\hat{\mathbf{n}}_{ij}$ is the normalized area-normal vector. Nishikawa [9] called the term in the brackets as damping term. The edge-normal augmentation leads to a non-robust scheme on highly-skewed meshes using the cell-centered grid metric. With the edge-normal augmentations, the damping-term contributions to the diffusion operator vanish when $\hat{\mathbf{n}}_{ij} \cdot \hat{\mathbf{e}}_{ij}$ approaches zero. With the face-tangent augmentation, the damping-term contributions are always large, preventing the odd-even

decoupling. It has been observed that, in many cases, a converged cell-centered solution is obtained only with the face-tangent augmentation.

The Green-Gauss (GG) and least-squares (LSQ) approaches for cell-gradient calculation are widely used. For second-order accuracy, the cell-gradient is assumed to be constant over the control volume.

Following the Green-Gauss theorem, the cell gradient is approximated as a discrete surface integral, a sum of scalar values reconstructed at the face-integration point multiplied by the area-normal face vector

$$\nabla W_i = \frac{1}{\Omega_i} \sum_{j=1}^{N} \frac{1}{2} (W_i + W_j) \cdot \mathbf{n}_{ij}. \tag{8}$$

Because of the approximation properties of the cell-vertex integration scheme [5, 9], the GG gradient is exact for a linear function only on tetrahedral or triangular meshes, although reasonable accuracy has been demonstrated in computations on mixed grids [8]. For the cell-centered metric, the GG gradient is not generally exact for a linear function; accuracy is achieved only if the edge-midpoint coincides with the face-integration point [8].

The LSQ cell-gradient [1] is computed by solving a system of linear equations for the gradient values. The system results from the minimization of the functional

$$\sum_{j=1}^{N} w_{ij}^2 \left(\nabla W_i \cdot \left(\mathbf{x_j} - \mathbf{x_i} \right) - (W_j - W_i) \right)^2 \rightarrow \min. \tag{9}$$

Here x_i is the coordinate vector of point i and w_{ij} is a weighting factor chosen as $w_{ij} = 1/\left|\mathbf{x_j} - \mathbf{x_i}\right|$. This weighted LSQ method is known to improve gradient accuracy on certain high aspect ratio grids [4, 8] due to an improvement of the condition of the linear system [8]. The LSQ cell-gradients represent linear functions exactly for cell-vertex and cell-centered discretizations. Mavriplis [8] noted that this is not a sufficient criterion for accuracy certification in the context of the whole finite volume scheme. The accuracy depends on the choice of the stencils for the LSQ minimization.

The LSQ stencil is the set of points involved in the sum of Eq. 9. A comprehensive study of inviscid finite-volume discretizations employing various LSQ stencils can be found in [4]. The nearest neighbor (NN) stencil includes only face-neighbors (Fig. 4(a)). The NN stencil is inexpensive, but does not necessarily provide accuracy and robustness [4, 8]. The full augmentation (FA) stencil includes all neighbors that share a vertex with the given volume (Fig. 4(b)). In an edge-based code, this extension beyond the face-neighbors is straightforward. The FA stencil normally leads to robust and accurate solutions but is expensive to compute [4], in particular in 3-D cases. The smart augmentation (SA) stencil employs only a small portion of the points used on the corresponding FA stencil (Fig. 4(c)). The SA stencil expands the NN stencil by one volume point per volume vertex. In this paper for each control volume vertex, the cell center added to the SA stencil is the nearest to the stencil center of all the cells surrounding the vertex.

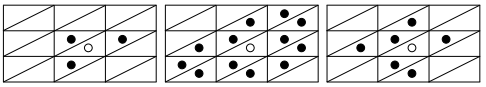

(a) NN (b) FA (c) SA

Fig. 4 Least-square gradient stencils for cell-centered grid metric. White circle represent computation points (stencil center), black circles represent neighbors involved in the stencil.

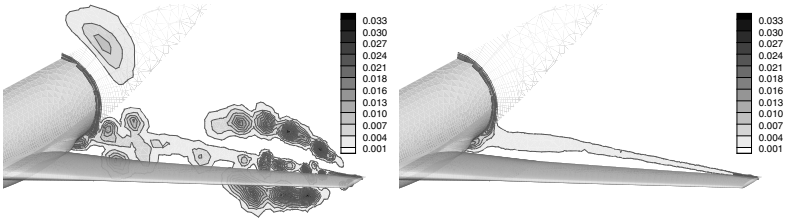

(a) SA stencil (b) cSA stencil

Fig. 5 Influence of the stencil of the least-squares gradient on the eddy-viscosity (plane behind the wing of the DLR-F6 configuration as in Fig. 1)

Fig. 6 Improved idealized drag polar compared to Fig. 1 for the cell-centered grid metric using second order upwind scheme, least-square gradient reconstruction based on the cSA stencil

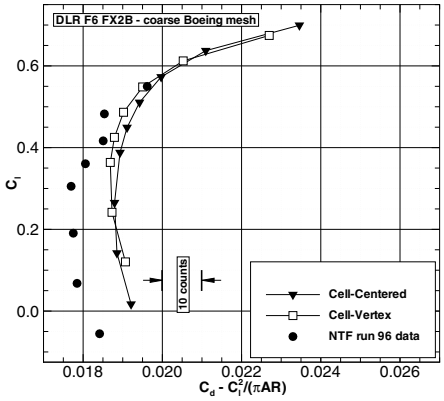

With this SA stencil, there still are instances, where additional points should be added to the stencil to provide accurate cell-gradients. Without sufficient cell-gradient accuracy, large errors are introduced to the turbulence equation through gradient sources [2], thus leading to erroneous eddy-viscosity. Non-physical vortex structures (Fig. 5(a)), which have their origins at elements with inaccurate gradients, can be observed. To prevent these non-physical vortex structures, the SA stencil is expanded by adding additional points from the FA-stencil. Points are added if their addition improves the condition number of the LSQ system. The Frobenius matrix norm is chosen to compute the condition number. The expanded stencil is denoted

as conditioned smart augmentation (cSA) stencil. With the cSA stencil, the non-physical vortex structures do not appear, see Fig. 5(b).

Fig. 6 shows that, with the upwind scheme using the LSQ cSA gradients, the large offset between cell-centered and cell-vertex polars has been completely removed. Note that the offset is removed even with the SA stencil; cSA stencil is required to remove the non-physical vortex structures.

4 Conclusions

Inaccuracy in the cell-centered version of the edge-based TAU-code has been observed, explained, and cured. The roots of inaccuracy are twofold: (1) large deviations between the locations of the face-integration point and the edge-midpoint on non-orthogonal meshes led to accuracy deterioration in computations with a central scheme or an upwind scheme using Green-Gauss gradients for convective fluxes. (2) inaccurate gradient computations led to erroneous turbulence sources and non-physical eddy viscosity. To cure these inaccuracies, an upwind scheme using the least-square gradients computed with a compact cSA stencil has been applied. Additionally, the robustness of computations has been improved by introduction of face-tangent augmentation for face-gradients used in viscous fluxes.

References

1. Barth, T.J.: A 3-D Upwind Euler Solver for Unstructured Meshes. AIAA Paper 91-1548 (1991)
2. Blazek, J.: Computational Fluid Dynamics: Principles and Applications. Elsevier, Amsterdam (2001)
3. Diskin, B., Thomas, L.T., Nielsen, E.J., Nishikawa, H., White, J.A.: Comparison of Node-Centered and Cell-Centered Unstructured Finite-Volume Discretizations: Viscous Fluxes. AIAA Journal 48(7), 1326–1338 (2010) (Also AIAA 2010-597)
4. Diskin, B., Thomas, L.T.: Comparison of Cell-Centered and Node-Centered Unstructured Finite-Volume Discretizations: Inviscid Fluxes. In: 48th AIAA Aerospace Sciences Meeting, AIAA 2010-1079, Orlando, FL (January 2010)
5. Diskin, B., Thomas, L.T.: Accuracy Analysis of Mixed Element Finite Volume Discretization Schemes. NIA Report 2007-08, National Institute of Aerospace, Hampton, VA 23681, USA (August 2007)
6. Haselbacher, A., Blazek, J.: On the Accurate and Efficient Discretisation of the Navier-Stokes Equations on Mixed Grids. AIAA Paper 98-0612 (1998)
7. Mavriplis, D.J.: Aerdodynamic drag prediction using unstructured mesh solvers. In: Deconoinck, H., Sermus, K., van Dam, C. (eds.) CFD-Based Drag Prediction and Reduction, von Karman Institute for Fluid Dynamics, Rhode St-Genese, Belgium, March. VKI Lecture Series 2003-02 (2003)
8. Mavriplis, D.J.: Revisiting the Least-squares Procedure for Gradient Reconstruction on Unstructured Meshes. In: 16th AIAA CFD Conference, AIAA 2003-3986, Orlando, FL (June 2003)

9. Nishikawa, H.: Beyond Interface Gradient: A General Principle for Constructing Diffusion Schemes. In: 40th Fluid Dynamic Conference and Exhibit, AIAA Paper 2010-5093, Chicago, Illinois (June 2010)
10. Schwamborn, D., Gerhold, T., Heinrich, R.: The DLR TAU-Code: Recent Applocations in Research and Industry. In: ECCOMAS CFD 2006 Conference, Netherlands (2006)
11. Thomas, L.T., Diskin, B., Nishikawa, H.: A Critical Study of Agglomeration Multigrid for Diffusion oh Highly Stretched Grids. Computers and Fluids (2010) (published electronically), doi: 10.1016/j.compfluid.2010.09.023
12. Vassberg, J., Broderson, O., Wahls, R., Zickuhr, T., Mavriplis, D., Tinoco, E., Mani, M., Levy, D., Eisfeld, B., Murayama, M., Morrison, J.: Comparison of NTF experimental data WITH CFD predictions from Third AIAA Drag Prediction Workshop, AIAA Paper 2008-6918 (January 2008)